NUMERICAL METHODS FOR GENERAL RELATIVISTIC MAGNETOHYDRODYNAMICS

by

Nicholas J. Nelson

A senior thesis submitted to the faculty of

Brigham Young University

in partial fulfillment of the requirements for the degree of

Bachelor of Science

Department of Physics and Astronomy

Brigham Young University

April 2007

BRIGHAM YOUNG UNIVERSITY

DEPARTMENT APPROVAL

of a senior thesis submitted by

Nicholas J. Nelson

This thesis has been reviewed by the research advisor, research coordinator, and department chair and has been found to be satisfactory.

Date	David Neilsen, Advisor
Date	Eric Hintz, Research Coordinator
Date	Scott D. Sommerfeldt, Chair

ABSTRACT

NUMERICAL METHODS FOR GENERAL RELATIVISTIC MAGNETOHYDRODYNAMICS

Nicholas J. Nelson

Department of Physics and Astronomy

Bachelor of Science

Potential numerical methods for solving the general relativistic magnetohydrodynamic (GRMHD) fluid equations are investigated. Specifically, a one dimensional central weighted essentially non-oscillatory (CWENO) scheme without a staggered grid and a one dimensional weighted essentially non-oscillatory (WENO) scheme are discussed in the context of solving the relativistic fluid equations. The implementation of CWENO and WENO are described, and both are applied to standard test problems. The modified CWENO scheme is found to be unstable in tests using the GRMHD fluid equations and Burger's equation. When solving the general relativistic perfect fluid equations, WENO is stable and has sharp resolution of shocks.

ACKNOWLEDGMENTS

I would like to acknowledge my wife, Rachel Nelson, without whose support, this work would not have been possible. I thank Dr. David Neilsen for his guidance and invaluable assistance. I acknowledge the Office of Research and Creative Activities at Brigham Young University and the National Science Foundation (NSF PHY-0502218) for their financial support.

Contents

List of Figures

Chapter 1

Introduction

1.1 Astophysics and Numerical Modeling

1.1.1 Understanding Observational Phenomena

With ground-breaking advances in observational technology such as space-based telescopes, high-energy electromagnetic observatories, and gravitational wave detectors, many new and interesting celestial objects have now become accessible for study (for further details, see [1]). In the electromagnetic spectrum, the Swift satellite can observe gamma ray bursts, and the Chandrasekhar X-ray Observatory satellite can study active galactic nuclei in great detail. Gravitational wave detectors, such as the Laser Interferometer Gravitational Wave Observatory (LIGO), provide the opportunity to correlate electromagnetic and gravitational observation efforts for the first time, allowing for even more observational data on some of the most energetic events in the universe.

Two very interesting astrophysical phenomena are active galactic nuclei and gamma ray bursts. Active galactic nuclei (AGN) are believed to be rotating supermassive black holes at the center of galaxies that are surrounded by a disk of matter taken

from nearby stars and the interstellar medium. The rotating black hole creates a strong magnetic field in the accretion disk that columnates the x ray emission from the AGN. Once captured, this matter begins to be accreted onto the black hole. The rotating black hole creates a strong magnetic field in the accretion disk. In this configuration, energy from the rotating accretion disk is extracted and emitted as jets of x rays along the axis of rotation through the Blandford-Znajek process [2]. AGNs are some of the strongest sources of x ray radiation in the sky. Gamma-ray bursts (GRB) are some of the most energetic explosions in the universe. A number of theories have offered descriptions of GRBs [3], one of which involves a collision between neutron stars with strong magnetic fields or between a magnetic neutron star and a black hole. In both cases, the theoretical framework for understanding these events is general relativistic magnetohydrodynamics (GRMHD).

1.1.2 Computational Models

As phenomena such as accretion disks around active galactic nuclei and gamma-ray bursts can now be studied observationally, there is an increased need for computational work to connect observational data with detailed models using fundamental physics. Due to the nonlinear nature of astrophysical systems, analytical methods fail to completely describe the physical mechanisms present in AGNs and GRBs. The nonlinear nature of these problems favors the use of numerical methods.

The overall goal of the work in this area at BYU is to develop a numerical code capable of modeling the collision of a black hole/neutron star system from long-range gravitational interaction, through the inspiral phase and the tidal decomposition of the star to the formation of an accretion disk. One of the major challenges in this endeavor is to create a numerical code capable of solving the GRMHD fluid equations over a wide range of dynamical and physical scales. The GRMHD fluid equations are

genuinely non-linear and therefore produce shock waves and other complex features. In this thesis, we will focus on describing and testing high-resolution shock-capturing numerical methods for use in numerical simulations of AGNs and GRBs.

1.2 The GRMHD equations

1.2.1 Introduction

To study processes around a black hole requires general relativistic magnetohydrodynamics (GRMHD). The GRMHD fluid equations model the matter and electromagnetic fields in an accretion disk or neutron star, while general relativity provides the gravitational interactions between the disk or star and the accompanying black hole as well as the gravitational self-interaction of the disk or star. GRMHD has already been used to study a wide variety of astrophysical objects [4–9].

The equations to be solved in the numerical model can be placed into two groups. The first group are the Einstein equations. These form a system of ten coupled partial differential equations. The ability to solve them effectively is extremely important, but falls outside of the scope of this thesis. The Einstein equations are typically split in the Arnowitt, Deser and Misner (ADM) 3+1 formulation [10], which formulates the equations as an initial value problem. We will mention the tensor form of the equations only and focus on the stress-energy tensor. The Einstein equations are

$$G_{ab} = 8\pi T_{ab}, \tag{1.1}$$

where units are chosen such that $G = 1$ and $c = 1$.

The Einstein equations relate spacetime, governed by G_{ab}, to the matter and energy present, represented by T_{ab}. The formulation of the stress-energy tensor, as done in [11] and [12], is made by combining a perfect fluid with an electromagnetic

field. The stress-energy tensor is formulated for a GRMHD fluid by utilizing the ideal magnetohydrodynamic assumption, which states that the electric field in the frame of the fluid is zero everywhere. Essentially, we are assuming that the fluid is a perfect conductor, where charged particles can move freely. In this environment, any electric field would be eliminated by a redistribution of charged particles.. This condition is also sometimes referred to as the "lock-in" condition, as the magnetic field lines are stationary in the reference frame of the fluid. The MHD stress-energy tensor is

$$T_{ab} = \left(\rho_0 \left(1+\epsilon\right) + P + b_c b^c\right) u_a u_b + \left(P + \frac{1}{2} b_c b^c\right) g_{ab} - b_a b_b. \tag{1.2}$$

The fluid described by Eq. (1.2) is characterized by the internal energy of the fluid ϵ, the rest-frame density ρ_0, the pressure P, the four-velocity u_i, the magnetic field b_i, and the metric g_{ij}.

1.2.2 The GRMHD Fluid Equations

The fluid equations are given by $\nabla_b T^b{}_a = 0$. A more complete description of the fluid equations can be found in [11]. The fluid equations are best solved numerically in terms of variables which have conservation properties, rather than the variables used in Eq. (1.2). The variables used in Eq. (1.2) are referred to as the primitive variables, while those that will be evolved in the fluid equations are called the conserved variables. We relate the conserved variables to the primitive variables as shown in Eqs. (1.3)–(1.6).

$$D = W\rho_0 \tag{1.3}$$

$$S_i = \left(h_e W^2 + B^2\right) v_i - \left(B^j v_j\right) B_i \tag{1.4}$$

$$\tau = h_e W^2 + B^2 - P - \frac{1}{2}\left[\left(B^j v^j\right)^2 + \frac{B^2}{W^2}\right] \tag{1.5}$$

$$B_i = -W b_i + v_i n^j b_j \tag{1.6}$$

The conserved variables are the relativistic density D, momentum S_i, and energy $E = \tau + D$, where τ is a variable that is roughly analogous to kinetic energy. The final conserved variable is the magnetic field in an observing reference frame, B_i. In Eqs. (1.3)–(1.6), we use the magnetic field magnitude $B^2 = B^i B_i$, the fluid enthalpy $h_e = \rho_0 (1 + \epsilon) + P$, and the Lorentz factor $W = (1 - v^i v_i)^{-\frac{1}{2}}$, with latin indexes running over only spatial components. It should be noted that Eqs. (1.3)–(1.5) produce transcendental equations when solved for the primitive variables.

We write the fluid equations in terms of the conserved variables. However, as seen below, it is impossible to completely eliminate the primitive variables from the GRMHD fluid equations. The fluid equations are

$$\partial_t D + \partial_i \left(D v^i \right) = 0, \tag{1.7}$$

$$\begin{aligned} \partial_t S_b \quad & + \partial_i \left[S_b v^i + P h^i{}_b - \tfrac{1}{W^2} \left(B^i B_b - \tfrac{1}{2} h^i{}_b B^j B_j \right) \right] \\ & - \partial_i \left[\tfrac{1}{2} B^j v_j \left(B^i v_b - \tfrac{1}{2} h^i{}_b B^j v_j \right) \right] = 0 \end{aligned}, \tag{1.8}$$

$$\partial_t \tau + \partial_i \left(S^i - v^i D \right) = 0, \tag{1.9}$$

$$\partial_t B^b + \partial_i \left(B^b v^i - B^i v^b \right) = 0, \tag{1.10}$$

$$\partial_i B^i = 0. \tag{1.11}$$

To complete the system of equations, a polytropic equation of state is used, where $P = (\Gamma - 1) \rho_o \epsilon$ and Γ is the adiabatic index. The equations form a system of eight coupled partial differential equations in conservation law form, suitable for a high-resolution shock-capturing scheme. The only exception is Eq. (1.11), which is the "no monopoles" constraint and is not solved directly. At this point, the equations are ready for an initial data, boundary conditions, and numerical evolution.

1.3 High-resolution shock-capturing methods

1.3.1 Essentially non-oscillatory schemes

High-resolution shock-capturing (HRSC) methods are a class of numerical methods for evolving genuinely non-linear equations. While there are a number of HRSC methods, this thesis will focus on essentially non-oscillatory (ENO) schemes for computing spatial derivatives. ENO schemes are designed to suppress unphysical oscillations that tend to appear preceding and following shock waves by dynamically adapting the method for approximating spatial derivatives using the local smoothness of the solution.

The GRMHD fluid equations are genuinely nonlinear and discontinuities arise from generic smooth initial data. Standard finite difference schemes produce oscillations preceding and following discontinuities. These oscillations, if left unchecked, grow in time and will drown out any fine features of the solution very quickly. Shu gives a detailed overview of a number of ENO schemes [13]. This thesis will detail two such schemes: a central weighted essentially non-oscillatory scheme (CWENO) and a weighted essentially non-oscillatory scheme (WENO) and compare them to a third schemes, a central essentially non-oscillatory scheme (CWENO) [13].

1.3.2 Time Integration

The fluid equations are discretized in time using the method of lines to decouple the time derivative from the spatial derivatives. This allows us to mix and match schemes for the temporal and spatial derivatives. The focus of this thesis will on methods for dealing with the spatial derivatives, but it is important to briefly discuss the method for time integration as well.

In order to avoid losing the non-oscillatory properties of the ENO methods, a

third order total variation diminishing (TVD) Runge-Kutta method is used to evolve the equations in time. Total variation diminishing Runge-Kutta schemes are designed specifically to preserve the non-oscillatory properties of ENO and other HRSC methods. The third-order, TVD Runge-Kutta method used in this thesis was developed by Shu and Osher [14]

$$\vec{u}^{(1)} = \vec{u}^n + \Delta t L\left(\vec{u}^n\right) \tag{1.12}$$

$$\vec{u}^{(2)} = \frac{3}{4}\vec{u}^n + \frac{1}{4}\vec{u}^{(1)} + \frac{1}{4}\Delta t L\left(\vec{u}^{(1)}\right) \tag{1.13}$$

$$\vec{u}^{(1)} = \frac{1}{3}\vec{u}^n + \frac{2}{3}\vec{u}^{(2)} + \frac{2}{3}\Delta t L\left(\vec{u}^{(2)}\right). \tag{1.14}$$

With the use of a TVD scheme for time derivatives, the benefits of ENO schemes can be fully utilized.

1.4 Summary of results

This thesis is organized in the following manner. First, we will present the implementation, testing, and results of our work with a CWENO scheme. The CWENO scheme uses a staggered grid, however our numerical code does not allow for a staggered grid. Our implementation modifies the CWENO scheme in that it does not use a staggered grid. We present the details of the CWENO scheme that we used and the results of some initial test problems. Unfortunately, CWENO schemes without a staggered grid prove to be inherently unstable for the GRMHD fluid equations. We also present some tests done with Burger's equations comparing CWENO and CENO.

The second major topic in this thesis will be presenting the formulation, implementation, and initial testing of a WENO scheme with characteristic decomposition. We give a detailed description of the implementation of a WENO scheme. Since the eigenvectors for the full GRMHD equations are not currently known in a computationally usable form, the WENO scheme will be used to solve the general relativistic fluid

equations with no magnetic field. When WENO is applied to the general relativistic perfect fluid equations, it shows notable improvements in resolving discontinuities over CENO. However, WENO also proves to be much more computationally expensive than CENO. In spite of the additional computational cost, WENO is shown to be a potentially suitable method for solving the GRMHD fluid equations as part of a project to model a black hole/neutron star collision.

Chapter 2

Numerical Methods

2.1 The Essentially Non-Oscillatory Philosophy

Genuinely non-linear equations, such as the GRMHD fluid equations, tend to produce discontinuities for almost all smooth initial data. Discontinuous solutions are extremely problematic for finite difference schemes because without the assumption of smoothness, we lose the notion of a derivative. Standard finite difference schemes tend to produce strong, unphysical oscillations near discontinuities. Essentially non-oscillatory (ENO) schemes were introduced in the late 1980's to deal with this problem. For a summary of a variety of ENO schemes, see [13].

The original ENO scheme uses the philosophy that by adapting which points a finite difference method uses, one can avoid approximating derivatives over discontinuities. These adaptive stencils are designed to only use points on one side of the discontinuity or the other. In this way, derivatives are never taken across a discontinuity. Many of the early ENO schemes are designed to work with characteristic variables, and thus require a spectral decomposition using the eigenvalues and eigenvectors of the Jacobian matrix.

After the introduction of the original ENO scheme, another version was developed known as a weighted essentially non-oscillatory (WENO) scheme. Like ENO, WENO uses adaptive stencils as well as the spectral or characteristic decomposition, to sharpen shocks. WENO differs from ENO mainly in the way it handles the adaptive stencils. ENO uses logic to decide which stencil to use, while WENO uses all of the stencils combined in a weighted sum. WENO combines the values from each stencil using a system of weights that are designed to eliminate the contribution from stencils with discontinuities. In this way, WENO is more efficient in smooth regions than ENO, while maintaining many of the same benefits.

Both the original ENO scheme and WENO use characteristic decompositions. In many systems, such as the GRMHD fluid equations, eigenvectors and eigenvalues are difficult to calculate and implement numerically. Central ENO schemes have been developed that do not require the characteristic decomposition. One such scheme is a central weighted essentially non-oscillatory (CWENO) scheme. CWENO uses the same adaptive stencil philosophy as WENO, but does not require characteristic decomposition. CWENO is a finite volume scheme formulated for use with staggered grids. CWENO looses some accuracy near shocks as a result, but is much less computationally expensive than WENO. Our CENO reference scheme is also a central method [13].

2.2 CWENO

We implemented CWENO as part of a numerical code designed to solve the GRMHD equations and as part of a numerical code to solve Burger's equation (see Eq. (3.1)). Both numerical codes used a non-staggered grid. For a more general and detailed description of CWENO and other ENO schemes, see [13] and [15].

2.2.1 System of Conservation Law Equations for GRMHD Fluid Equations

CWENO is a high resolution, shock capturing scheme for computing spatial derivatives in conservation law schemes.

$$\partial_t \vec{U} + \partial_i \vec{F}^i = 0. \tag{2.1}$$

The flat space fluid equations in conservation form are given by

$$\vec{U} = \begin{bmatrix} D \\ S_b \\ \tau \\ B_b \end{bmatrix} \tag{2.2}$$

and

$$\vec{F}\left(\vec{U}\right)^i = \begin{bmatrix} Dv^i \\ S_b v^i + P h_b^i - \frac{1}{W^2}\left(B^i B_b - \frac{1}{2} h_b^i B^j B_j\right) - \frac{1}{2} B^j v_j \left(B^i v_b - \frac{1}{2} h_b^i B^j v_j\right) \\ S^i - v^i D \\ B_b v^i - B^i v_b \end{bmatrix}. \tag{2.3}$$

The fluid equations are discretized in time using the method of lines, and the semi-discrete equations are

$$\frac{dU_j}{dt} = -\frac{\hat{F}_{j+1/2} - \hat{F}_{j-1/2}}{\Delta x} \tag{2.4}$$

where the index j labels points on a discrete grid of $N + 1$ points.

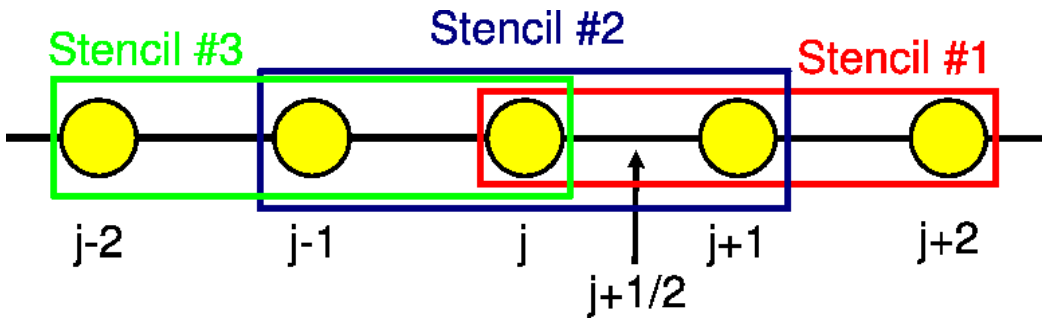

Figure 2.1 Stencils used by fourth-order CWENO and WENO reconstruction routines to compute the value of $\vec{U}^L_{j+1/2,r}$. The stencils for $\vec{U}^R_{j+1/2,r}$ are symmetric about $j+1/2$.

2.2.2 Numerical Fluxes

The numerical flux vectors $\hat{F}_{j+1/2}$ and $\hat{F}_{j-1/2}$ are calculated using the Lax-Friedrichs flux given by

$$\hat{F}_{j+1/2} = \frac{1}{2}\left[\vec{F}\left(\vec{U}^L_{j+1/2}\right) + \vec{F}\left(\vec{U}^R_{j+1/2}\right) - \left(\vec{U}^R_{j+1/2} - \vec{U}^L_{j+1/2}\right)\right]. \tag{2.5}$$

This requires the fluxes to be computed between grid points from both the right side and the left side; however the values of the conserved and primitive variables are known only at the grid points. The process of calculating the values at $x_{j+1/2}$ from both sides is called reconstruction.

The numerical fluxes depend entirely on the left and right reconstructed values of $\vec{U}_{j+1/2}$, $\vec{U}^L_{j+1/2}$ and $\vec{U}^R_{j+1/2}$ respectively. The reconstruction method determines the order of accuracy that the scheme can achieve. The CWENO method uses a series of adaptive stencils to compute the value of $\vec{U}^L_{j+1/2}$ and $\vec{U}^R_{j+1/2}$. For fifth-order accuracy in smooth regions, the CWENO algorithm computes three second-order polynomials using three different stencils from the right side of $x_{j+1/2}$, as shown in Fig. 2.1. Three symmetrical stencils are used for the reconstruction of the left side of $x_{j+1/2}$ as well. The three values for $\vec{U}^L_{j+1/2}$ and $\vec{U}^R_{j+1/2}$ are denoted by $\vec{U}^L_{j+1/2,r}$ and $\vec{U}^R_{j+1/2,r}$, where $r = 0, 1, .., d$ and $r = 0$ corresponds to the right-most stencil. Increasing r moves the

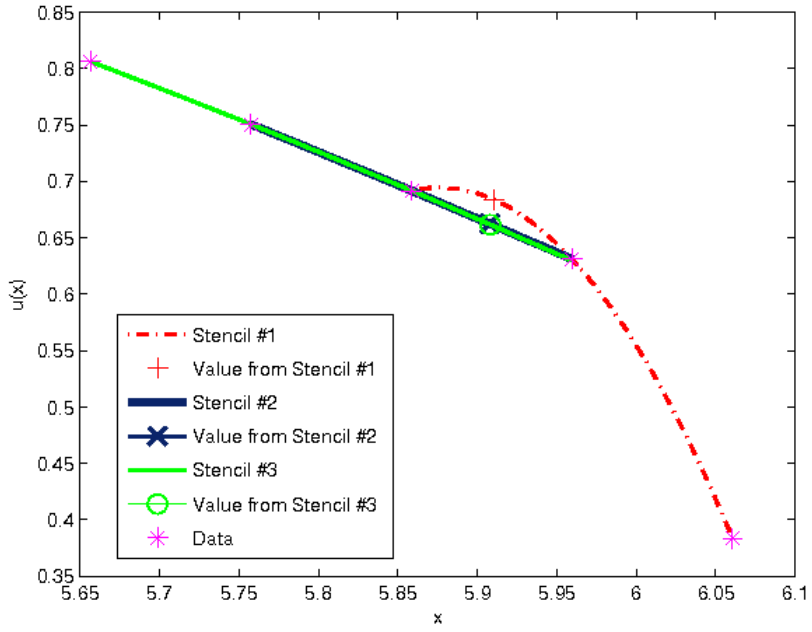

Figure 2.2 Quadratic reconstructions of $\vec{U}^L_{j+1/2,r}$ for arbitrary data with a discontinuity. Note that stencils number two and three provide accurate (almost identical) values for $U^L_{j+1/2}$. Stencil number one, however, contains the discontinuity and gives an inaccurate reconstructed value.

stencils to the left.

The scheme can be generalized to higher orders, but in this thesis we will present only a fifth-order scheme, where $d = 3$. To compute $\vec{U}^L_{j+1/2,r}$ and $\vec{U}^R_{j+1/2,r}$, we use

$$\vec{U}^L_{j+1/2,r} = \sum_{k=0}^{2} c_{r,k}\vec{U}_{j-r+k} \tag{2.6}$$

and

$$\vec{U}^R_{j+1/2,r} = \sum_{k=0}^{2} \bar{c}_{r,k}\vec{U}_{j-r+k+1}. \tag{2.7}$$

The matrices $c_{r,k}$ and $\bar{c}_{r,k}$ provide the coefficients for computing the quadratic polynomials for each stencil and evaluating that polynomial at $x_{j+1/2}$. The matrices are related in that $c_{r,k} = \bar{c}_{r-1,k}$. The constant matrix is obtained by assuming uniform grid size and using the Lagrange method for finding the interpolating polynomial.

This method yields

$$c_{m,n} = \begin{bmatrix} 11/6 & -7/6 & 1/3 \\ 1/3 & 5/6 & -1/6 \\ -1/6 & 5/6 & 1/3 \\ 1/3 & -7/6 & 11/6 \end{bmatrix}. \tag{2.8}$$

In $c_{m,n}$, $m = -1, ..., 2$ and $n = 0..2$. A sample reconstruction for $\vec{U}^L_{j+1/2,r}$ can be found in Fig. 2.2.

Having calculated $\vec{U}^L_{j+1/2,r}$ and $\vec{U}^R_{j+1/2,r}$, the processes for left and right reconstruction become identical, so we will drop the superscripts. Now we must combine the three third-order reconstructed values in such a way as to produce a fifth order scheme for smooth regions. CWENO must also avoid using stencils with discontinuities, which is accomplished through the use of smoothness indicators and non-linear weights.

2.2.3 Smoothness indicators and non-linear weights

The CWENO algorithm computes smoothness indicators for each of the quadratic reconstructions preformed in Eqs. (2.6) and (2.7). Smoothness indicators essentially measure the size of the L_2 norm of the first and second derivatives of the polynomials used to compute $\vec{U}_{j+1/2}$. These smoothness indicators are then used to calculate non-linear weights for each stencil. The value of $\vec{U}_{j+1/2}$ is then calculated by summing over $\vec{U}_{j+1/2,r}\vec{w}_r$, where w_r are the non-linear weights. For a more thorough and general treatment, see [13].

The smoothness indicators $\vec{s}_r$ for a fourth-order scheme are computed for each of the stencils using

$$\vec{s}_0 = \frac{13}{12}\left(\vec{U}_j - 2\vec{U}_{j+1} + \vec{U}_{j+2}\right)^2 + \frac{1}{4}\left(3\vec{U}_j - 4\vec{U}_{j+1} + \vec{U}_{j+2}\right)^2, \tag{2.9}$$

$$\vec{s}_1 = \frac{13}{12}\left(\vec{U}_{j-1} - 2\vec{U}_j + \vec{U}_{j+1}\right)^2 + \frac{1}{4}\left(\vec{U}_{j-1} - \vec{U}_{j+1}\right)^2, \tag{2.10}$$

and

$$\vec{s}_2 = \frac{13}{12}\left(\vec{U}_{j-2} - 2\vec{U}_{j-1} + \vec{U}_j\right)^2 + \frac{1}{4}\left(\vec{U}_{j-2} - 4\vec{U}_{j-1} + 3\vec{U}_j\right)^2. \tag{2.11}$$

The smoothness indicators are designed so that $s_r = O\left(\Delta x^2\right)$ if U is smooth in the given stencil and $s_r = O\left(1\right)$ if U has a discontinuity in the given stencil (from x_{j-r} to x_{j-r+2}). From the smoothness indicators, CWENO computes the non-linear weights using

$$a_r = \frac{d_r}{\left(\epsilon + s_r\right)^2} \tag{2.12}$$

and

$$w_r = \frac{a_r}{\sum_{l=0}^{2} a_l}. \tag{2.13}$$

In Eqs. (2.12)–(2.13), a_r is simply a place holder and d_r is a vector of pre-determined constants. The constants for a fourth order scheme are given by

$$d_r = \begin{pmatrix} 3/10 & 3/5 & 1/10 \end{pmatrix}. \tag{2.14}$$

The construction of d_r shows obvious preference to the central stencil. We should also note that while we have represented a_r and w_r as scalars, they are, in fact, vector components for a system of equations where each component is computed in exactly the same way.

With the non-linear weights computed, the values of $\vec{U}^L_{j+1/2}$ and $\vec{U}^R_{j+1/2}$ can now be computed via Eq. (2.15) by simply changing the superscript for the left and right reconstructions. Therefore,

$$\vec{U}_{j+1/2} = \sum_{r=0}^{2} \vec{w}_r \vec{U}_{j+1/2,r}. \tag{2.15}$$

We would also like to note that in Eq. (2.15), the multiplication is scalar multiplication between vector components.

2.2.4 Motivation for CWENO

For smooth data, CWENO combines the three quadratic reconstructions in a way that gives fifth-order accuracy. Since the scheme favors the central stencil above the other two, it helps avoid propagation errors that can cause wave speeds to artificially increase. CWENO does not use logical tests in reconstructing the states.

CWENO also possesses several important attributes for dealing with discontinuities that we can explore using the arbitrary scalar data from Fig. 2.2. It can be clearly seen that the reconstructed value for stencil one is being influenced by the discontinuity and is inaccurate. The smoothness indicators and non-linear weights for these data can be seen in Table 2.1.

	r	s_r	w_r
Stencil 1	0	0.1538	0.0140
Stencil 2	1	0.0510	0.7623
Stencil 3	2	0.0666	0.2237

Table 2.1 Smoothness indicators and non-linear weights for the arbitrary data in Fig. 2.2. The weight for stencil 1, which contains the discontinuity, is extremely small compared to the other two weights. CWENO has therefore effectively removed stencil 1 from the calculation.

Since w_0 is very small, CWENO is effectively using only stencils two and three and avoiding the stencil with the discontinuity. This prevents the formation of oscillations near discontinuities. Near the discontinuity, the order of accuracy drops when one or more stencils are not used. However, CWENO maintains higher orders of accuracy in smooth regions.

2.3 WENO

We also implement WENO as part of a numerical code designed to solve the GRMHD fluid equations. As discussed in the introduction to this chapter, WENO requires the use of eigenvectors and the eigenvectors for the GRMHD fluid equations, and these are not available for numerical implementation. However, eigenvectors are well known and available when the magnetic field is turned off [16]. The equations then reduce to the general relativistic perfect fluid equations. In order to study WENO, we implemented it into a numerical code that solves the general relativistic perfect fluid equations in flat space. For further details on the WENO scheme, see [13,17–19]. The work of Balsara and Shu [19] is especially helpful.

2.3.1 Introduction to WENO schemes

As with CWENO, WENO uses smoothness indicators and non-linear weights to create high-order schemes in smooth areas and avoid stencils with discontinuities. WENO uses the conservation law form given in equation (2.1) and the discretization used in equation (2.4). The method for computing the fluxes, however, is the starting point for the divergence from the method used by CWENO.

WENO computes the numerical fluxes using the right and left eigenvectors. The k-th right and left eigenvectors at $x_{j+1/2}$ are denoted by $\vec{r}_{k,x+1/2}$ and $\vec{l}_{k,j+1/2}$, respectively. The numerical fluxes at $x_{j+1/2}$, $\vec{F}_{j+1/2}$, are given by

$$\hat{F}_{j+1/2} = \sum_{k=1}^{m} \left(f^R_{k,j+1/2} + f^L_{k,j+1/2} \right) \vec{r}_{k,j+1/2}, \tag{2.16}$$

where $f^R_{k,j+1/2}$ and $f^L_{k,j+1/2}$ are the right and left flux components. It is important to note that in Eq. (3.1), the sum runs over the eigenvectors with the flux components acting like weights on the eigenvectors.

The method of constructing $f^R_{k,j+1/2}$ and $f^L_{k,j+1/2}$ determines the order of accuracy of the WENO scheme. In this thesis, we present a fourth-order scheme. The right flux component is defined in terms of the interpolating polynomials from the three right stencils, $q_{k,0}$, $q_{k,1}$, and $q_{k,2}$, and the left flux component is defined by the interpolated values from the three left stencils, $\bar{q}_{k,0}$, $\bar{q}_{k,1}$, and $\bar{q}_{k,2}$. The stencils are the same ones used in CWENO (see Fig. 2.1). The flux components are given by

$$f^R_{k,j+1/2} = \sum_{m=1}^{2} w_m q_{j+1/2,k,m}, \tag{2.17}$$

$$f^L_{k,j+1/2} = \sum_{m=1}^{2} \bar{w}_m \bar{q}_{j+1/2,k,m}, \tag{2.18}$$

where w_m and $\bar{w}_m$ are the non-linear weights and will be defined below.

The interpolated values q_m and $\bar{q}_m$ are given by

$$q_{j+1/2,k,m} = \sum_{n=0}^{2} c_{m,n} g_{j+1/2,k,j-m+n}, \tag{2.19}$$

$$\bar{q}_{j+1/2,k,m} = \sum_{n=1}^{3} \bar{c}_{m,n} \bar{g}_{j+1/2,k,j-m+n}, \tag{2.20}$$

where $c_{m,n}$ and $\bar{c}_m, n$ are the same as those used in CWENO [see Eq. (2.8)], and $g_{j+1/2,k,j-m+n}$ and $\bar{g}_{j+1/2,k,j-m+n}$ are flux components at $x_{j+1/2}$ extrapolated from x_{j-m+n}. The values for $g_{j+1/2,k,j-m+n}$ and $\bar{g}_{j+1/2,k,j-m+n}$ are given by

$$g_{j+1/2,k,j-m+n} = \frac{1}{2}\vec{l}_{k,j+1/2} \cdot \left(\vec{F}_{j-m+n} + \hat{\lambda}_{k,j+1/2}\vec{U}_{j-m+n}\right), \tag{2.21}$$

$$\bar{g}_{j+1/2,k,j-m+n} = \frac{1}{2}\vec{l}_{k,j+1/2} \cdot \left(\vec{F}_{j-m+n+1} - \hat{\lambda}_{k,j+1/2}\vec{U}_{j-m+n+1}\right), \tag{2.22}$$

where $\hat{\lambda}_{k,j+1/2}$ is the maximum eigenvalue. It is computed using

$$\hat{\lambda}_{k,j+1/2} = \chi \max\left(\left|\lambda_{k,j-2}\right|, \left|\lambda_{k,j-1}\right|, ..., \left|\lambda_{k,j+2}\right|\right). \tag{2.23}$$

The maximum eigenvalue is therefore simply the absolute value of the k-th eigenvalue with the greatest magnitude from the points that make up the three stencils used

(see Fig. 2.1). The value of χ is used to control the dissipation of the scheme and is generally set between 1.1 and 1.5.

With the interpolating polynomials defined, we can now turn our attention to computing the non-linear weights w_m and $\bar{w}_m$ mentioned in Eqs. (2.17)–(2.18). The method is identical to the one used in CWENO, except the smoothness indicators are computed from the values of g and $\bar{g}$, rather than the state variables. Therefore, for g, the smoothness indicators $\vec{s}_l$ are given by

$$\begin{aligned}\vec{s}_0 = \; & \tfrac{13}{12}\left(g_{j+1/2,k,j} - 2g_{j+1/2,k,j+1} + g_{j+1/2,k,j+2}\right)^2 \\ & + \tfrac{1}{4}\left(3g_{j+1/2,k,j} - 4\vec{g}_{j+1/2,k,j+1} + \vec{g}_{j+1/2,k,j+2}\right)^2,\end{aligned} \tag{2.24}$$

$$\begin{aligned}\vec{s}_1 = \; & \tfrac{13}{12}\left(g_{j+1/2,k,j-1} - 2g_{j+1/2,k,j} + g_{j+1/2,k,j+1}\right)^2 \\ & + \tfrac{1}{4}\left(g_{j+1/2,k,j-1} - g_{j+1/2,k,j+1}\right)^2,\end{aligned} \tag{2.25}$$

and

$$\begin{aligned}\vec{s}_2 = \; & \tfrac{13}{12}\left(g_{j+1/2,k,j-2} - 2g_{j+1/2,k,j-1} + g_{j+1/2,k,j}\right)^2 \\ & + \tfrac{1}{4}\left(g_{j+1/2,k,j-2} - 4g_{j+1/2,k,j-1} + 3g_{j+1/2,k,j}\right)^2.\end{aligned} \tag{2.26}$$

For $\bar{g}$, the smoothness indicators $\vec{t}_l$ are given by

$$\begin{aligned}\vec{t}_0 = \; & \tfrac{13}{12}\left(\bar{g}_{j+1/2,k,j} - 2\bar{g}_{j+1/2,k,j+1} + \bar{g}_{j+1/2,k,j+2}\right)^2 \\ & + \tfrac{1}{4}\left(3\bar{g}_{j+1/2,k,j} - 4\bar{g}_{j+1/2,k,j+1} + \bar{g}_{j+1/2,k,j+2}\right)^2,\end{aligned} \tag{2.27}$$

$$\begin{aligned}\vec{t}_1 = \; & \tfrac{13}{12}\left(\bar{g}_{j+1/2,k,j-1} - 2\bar{g}_{j+1/2,k,j} + \bar{g}_{j+1/2,k,j+1}\right)^2 \\ & + \tfrac{1}{4}\left(\bar{g}_{j+1/2,k,j-1} - \bar{g}_{j+1/2,k,j+1}\right)^2,\end{aligned} \tag{2.28}$$

and

$$\begin{aligned}\vec{t}_2 = \; & \tfrac{13}{12}\left(\bar{g}_{j+1/2,k,j-2} - 2\bar{g}_{j+1/2,k,j-1} + \bar{g}_{j+1/2,k,j}\right)^2 \\ & + \tfrac{1}{4}\left(\bar{g}_{j+1/2,k,j-2} - 4\bar{g}_{j+1/2,k,j-1} + 3\bar{g}_{j+1/2,k,j}\right)^2.\end{aligned} \tag{2.29}$$

The smoothness indicators are designed with the same properties as those for CWENO. From the smoothness indicators, WENO computes the non-linear weights w_r and $\bar{w}_r$ using

$$a_r = \frac{d_r}{(\epsilon + \vec{s}_r)^2}, \tag{2.30}$$

$$\bar{a}_r = \frac{d_{2-r}}{\left(\epsilon + \vec{t_r}\right)^2}, \tag{2.31}$$

$$w_r = \frac{a_r}{\sum_{l=0}^{2} a_l}, \tag{2.32}$$

and

$$\bar{w}_r = \frac{\bar{a}_r}{\sum_{l=0}^{2} \bar{a}_l}. \tag{2.33}$$

The constants d_r are the same as those for CWENO and are given in Eq. (2.14). It is also important to note that the stencils used for in Eqs. (2.21)–(2.22) are not the same. Anyone implementing this code must take care to use the values for $\vec{t}_m$ that correspond with the stencil covered by $\bar{q}_{j+1/2,k,m}$, which goes from x_{j-m+1} to x_{j-m+3}. With the non-linear wights computed, the algorithm is now complete.

2.3.2 Characteristic decomposition for perfect fluid model

The eigenvalues and eigenvectors for the general relativistic perfect fluid equations are given by Font et al in [16]. They are repeated here. First three eigenvalues are degenerate

$$\lambda_1 = \lambda_2 = \lambda_3 = \alpha v^x - \beta^x, \tag{2.34}$$

where α is the lapse function in the standard 3+1 formalism and β^x is the x component of the shift vector. In the case of flat space, which we will use for all calculations, $\alpha = 1$ and $\beta^i = 0$. In flat space, the spatial metric is simply $h_{ij} = \delta_{ij}$. The terms α, β^i, and h_{ij} are included in the equations for generality. The linearly independent eigenvectors for these three eigenvalues are

$$\vec{r}_1 = \left[\frac{k}{hW\left(k - \rho c_s^2\right)}, v_x, v_y, v_z, 1 - \frac{k}{hW\left(k - \rho c_s^2\right)}\right]^T, \tag{2.35}$$

$$\vec{r}_2 = h\left[\frac{Wv_y}{h}, h_{xy} + 2W^2 v_x v_y, h_{yy} + 2W^2 v_y^2, h_{yz} + 2W^2 v_z v_y, v_y W\left(2W - \frac{1}{h}\right)\right]^T, \tag{2.36}$$

$$\vec{r}_3 = h\left[\frac{Wv_z}{h}, h_{xz} + 2W^2 v_x v_z, h_{yz} + 2W^2 v_y v_z, h_{zz} + 2W^2 v_z v_z, v_z W\left(2W - \frac{1}{h}\right)\right]^T. \tag{2.37}$$

The remaining eigenvalues are

$$\lambda_\pm = \frac{\alpha}{1 - v^2 c_s^2}\left(v^x\left(1 - c_s^2\right) \pm \sqrt{c_s^2\left(1 - v^2\right)\left[h^{xx}\left(1 - v^2 c_s^2\right) - v^x v^x\left(1 - c_s^2\right)\right]}\right) - \beta^x \tag{2.38}$$

with the corresponding eigenvectors

$$\vec{r}_\pm = hW\left[\frac{1}{hW}, \left(v_x - \frac{v^x - \frac{\lambda_\pm + \beta^x}{\alpha}}{h^{xx} - v^x\frac{\lambda_\pm + \beta^x}{\alpha}}\right), v_y, v_z, \frac{h^{xx} - v^x v^x}{h^{xx} - v^x\frac{\lambda_\pm + \beta^x}{\alpha}} - \frac{1}{hW}\right]^T. \tag{2.39}$$

In the defining the eigenvectors and eigenvalues, we have used a number of calculated quantities to simplify the equations. In Eqs. (2.35)–(2.39),

$$k = \frac{\Gamma - 1}{\rho}, \tag{2.40}$$

$$h = 1 + \frac{P}{(\Gamma - 1)\rho} + \frac{P}{\rho}, \tag{2.41}$$

$$c_s^2 = \frac{P\Gamma}{h\rho}. \tag{2.42}$$

The eigenvectors calculated so far have been the right eigenvectors, or the column eigenvectors that satisfy the standard eigenvalue equation $A\vec{r}_i = \lambda^{(i)}\vec{r}_i$, where there is no implied sum over i. The left eigenvectors satisfy $\vec{l}_i A = \lambda^{(i)}\vec{l}_i$. The left eigenvectors are row vectors and are used in equation (2.21). In order to calculate the left eigenvectors, we create a matrix R whose columns are the right eigenvectors. A new matrix L is defined as the inverse of R, $L = R^{-1}$. The rows of L are then the left eigenvectors. Since matrix inversion in numerically expensive, the left eigenvectors are found analytically. A simple check for the process of calculating the left and right eigenvectors is that $\vec{r}_i \cdot \vec{l}_j = \delta_{ij}$.

With the eigenvectors for a general relativistic perfect fluid now calculated and the WENO method outlined, WENO is now fully defined and ready for testing. While

there are clear differences between the GRMHD equations and the general relativistic perfect fluid equations, both are genuinely non-linear and so the challenge of dealing with shocks and complex smooth features will still be present in our tests. WENO performance relative to a central scheme such as CENO will largely determine whether it would be advantageous to continue working on a numerically suitable formulation of the eigenvectors for the GRMHD fluid equations.

Chapter 3

Conclusions

3.1 Tests with CWENO

We test the CWENO scheme without a staggered grid using standard test problems for the inviscid Burger's equation and the GRMHD fluid equations.

3.1.1 CWENO applied to GRMHD equations

The first test for our modified CWENO algorithm is to compare it with another central ENO scheme called CENO. CENO has been used to successfully solve a number of problems using the GRMHD fluid equations. CWENO was chosen specifically for its similarities to CENO, however, we find that the modified CWENO scheme is unstable without a staggered grid. Specifically, CWENO on a non-staggered grid causes weak, slowly building instabilities in the GRMHD fluid equations. This instability occurs for all values of the Courant-Friedrichs-Lewy (CFL) parameter.

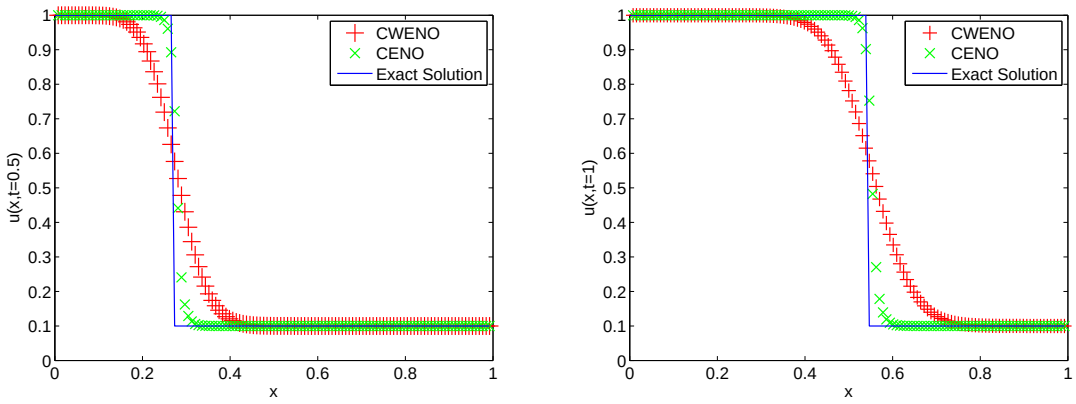

Figure 3.1 Exact solution, CENO solution, and CWENO solution for step function initial data at $t = 0.5$ (left) and $t = 1$ (right). In both figures, $\Delta x = \frac{1}{128}$ and $\Delta t = \frac{1}{256}$.

3.1.2 CWENO tests using Burger's Equation

To test the modified CWENO scheme, we studied the one-dimensional inviscid Burger's equation,

$$\frac{\partial}{\partial t}u(x,t) + \frac{c}{2}\frac{\partial}{\partial x}\left(u(x,t)^2\right) = 0, \tag{3.1}$$

where c is the wave speed.

Burger's equation, like the GRMHD fluid equations, is formulated as a conservation law and is genuinely non-linear. Burger's equation is also advantageous because exact solutions can be found. Specifically, we studied the use of CWENO for step-function initial data with constant boundary conditions. The results of this test are shown in Fig. 3.1. As can be seen in Fig. 3.1, CWENO resolves the shock fairly well. Although there is considerable smoothing that occurs, there are no oscillations produced in the vicinity of the discontinuity.

Compared to CENO, however, CWENO without a staggered grid performs quite poorly. Simulations were run with the same parameters used in Fig. 3.1 using both CWENO and CENO for step function initial data. The results were compared with the exact solution. Figure 3.2 shows the value of $\left|\left|U - \hat{U}\right|\right|_2$ as a function of time,

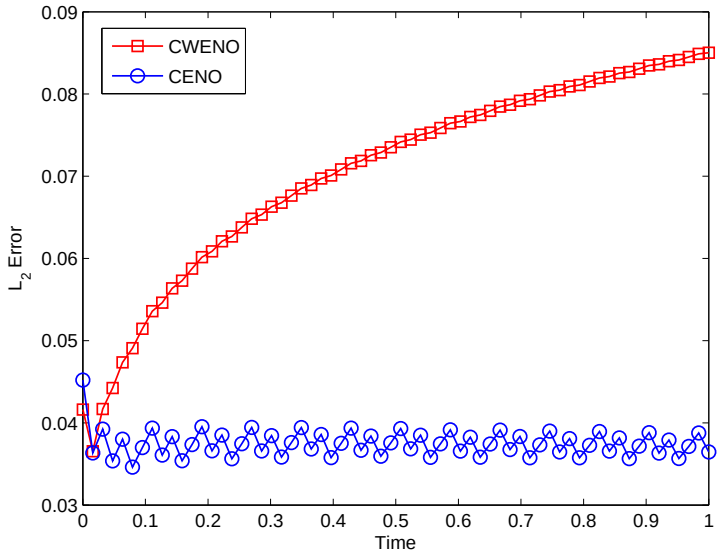

Figure 3.2 L_2 error in CWENO and CENO reconstructions as a function of time for Burger's equation with step-function initial data, constant boundary conditions, $\Delta x = \frac{1}{128}$, and $\Delta t = \frac{1}{256}$.

where U is the exact solution and $\hat{U}$ is the numerical solution.

Modified CWENO evidently does not produce superior results to CENO when dealing with sharp discontinuities. Also, CWENO without a staggered grid displays a troubling tendency in that the error increases in time, whereas CENO is roughly constant. The growth rate in the error is proportional to $\ln(t)$. While the growth rate is very small, it still blows up as time increases. Additional evolutions for longer times and with smaller CFL parameters have confirmed the existence of the growth in error. All data have shown the growth rate to be proportional to $\ln(t)$.

The increasing error in time for CWENO makes CENO a much better choice for solving Burger's equation. This small growth in error may also be the source of instability for the fluid equations, as they are much more sensitive to increasing error than Burger's equation. The instability seen in both Burger's equation and the GRMHD fluid equations indicates that CWENO will not be an effective method

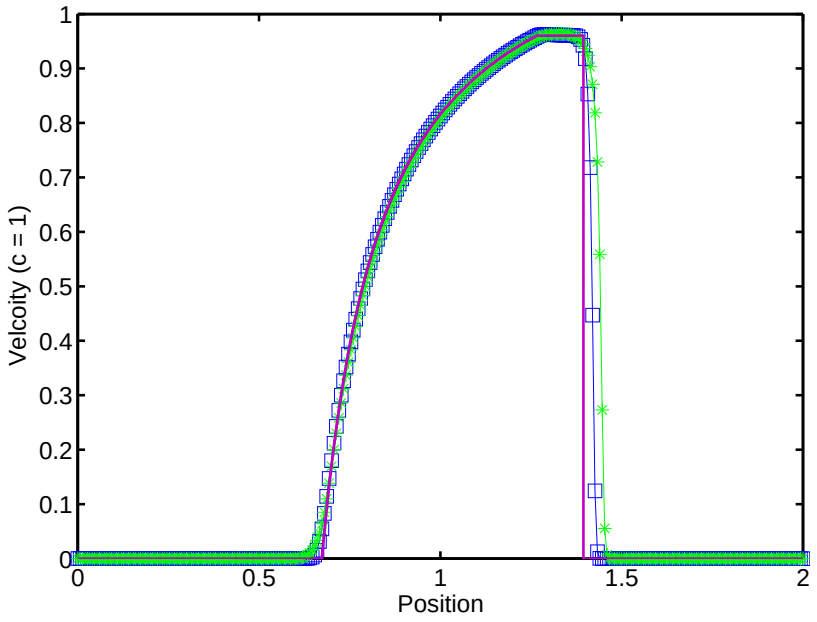

Figure 3.3 WENO and CENO solution for the velocity at $t = 0.4$ of the general relativistic perfect fluid equations for constant initial data in velocity and step function initial data where $v = 0$ for all x, $P = 1000$ for $x < 1$, and $P = 0.01$ for $x > 1$ at $t = 0$. This data was generated using $\Delta x = \frac{1}{150}$, $\Delta t = \frac{1}{375}$, and $\Gamma = \frac{5}{3}$. Figures 3.4, 3.5, and 3.6 were generated using these same parameters.

for solving the GRMHD equations and suggests that modified CWENO without a staggered grid may be weakly unstable for all discontinuous data.

3.2 Tests with WENO

We now apply WENO to the general relativistic perfect fluid equations, and once again use CENO for comparison purposes. Results from standard test problems show that WENO does a better job of resolving shocks than CENO. Figures (3.3)–(3.6) show the results from a standard shock-tube test problem, where the initial conditions are $\vec{v} = 0$, $\rho = 1$, $P = 1000$ for $x < 1$ and $P = 0.01$ for $x > 1$, and $\Gamma = \frac{5}{3}$.

As can be seen for the velocity, density, and pressure data, WENO does an excellent job of resolving discontinuities. For the velocity data in Fig. 3.3, WENO produces

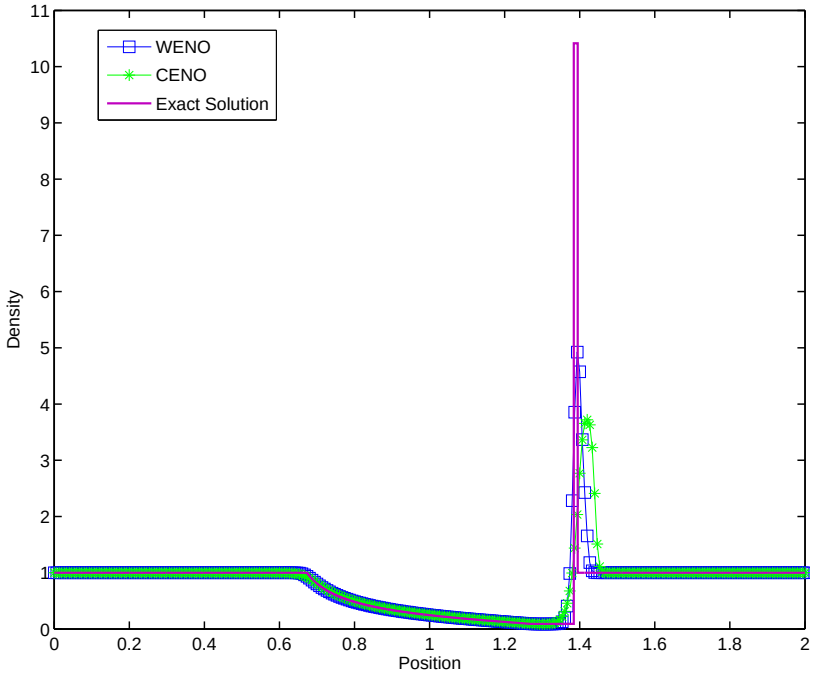

Figure 3.4 WENO and CENO solution for the density at $t = 0.4$ of the general relativistic perfect fluid equations for constant initial data in density and step function initial data, where $\rho = 1$ for all x, $P = 1000$ for $x < 1$, and $P = 0.01$ for $x > 1$ at $t = 0$.

a much sharper shock with a noticeably less rounded upper corner than CENO. This rounding of the upper edge of the shock wave leads to artificially increased propagation speeds. Because WENO produces a sharper shock, it has less artificial increase in propagation speed than CENO.

For the density data in Fig. 3.4, WENO does a better job of resolving the contact discontinuity that occurs when the shock wave encounters the unperturbed region. This region of extremely high density should have a small but finite width and discontinuities on both the leading a trailing edges. As the figure shows, WENO does a better job resolving the discontinuities and provides a better value for the density at the top of the high density region.

For the pressure data in Fig. 3.5, WENO also does a better job of resolving the shock than CENO. The discontinuity in pressure, which is shown in greater detail in

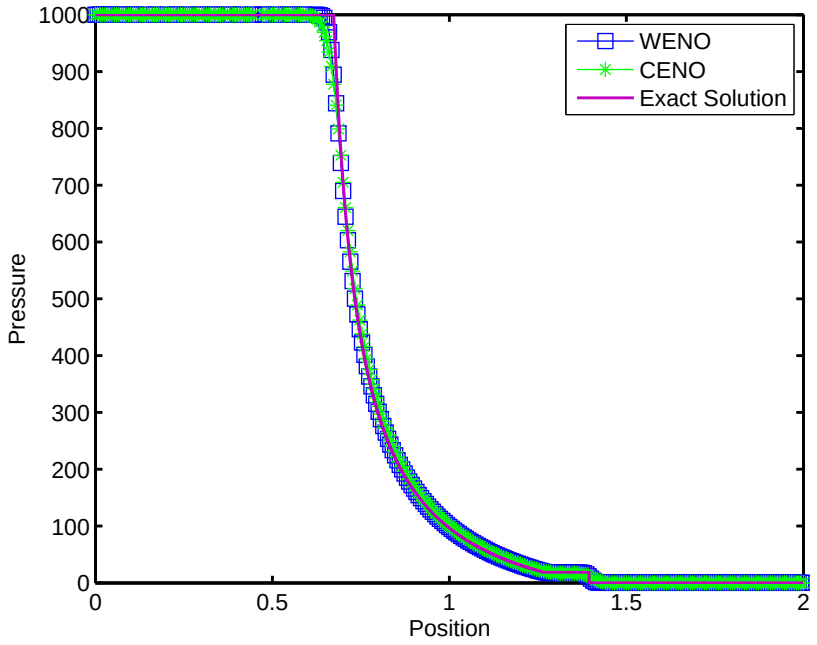

Figure 3.5 WENO and CENO solution for the density at $t = 0.4$ of the general relativistic perfect fluid equations for step function initial data where $P = 1000$ for $x < 1$ and $P = 0.01$ for $x > 1$ at $t = 0$.

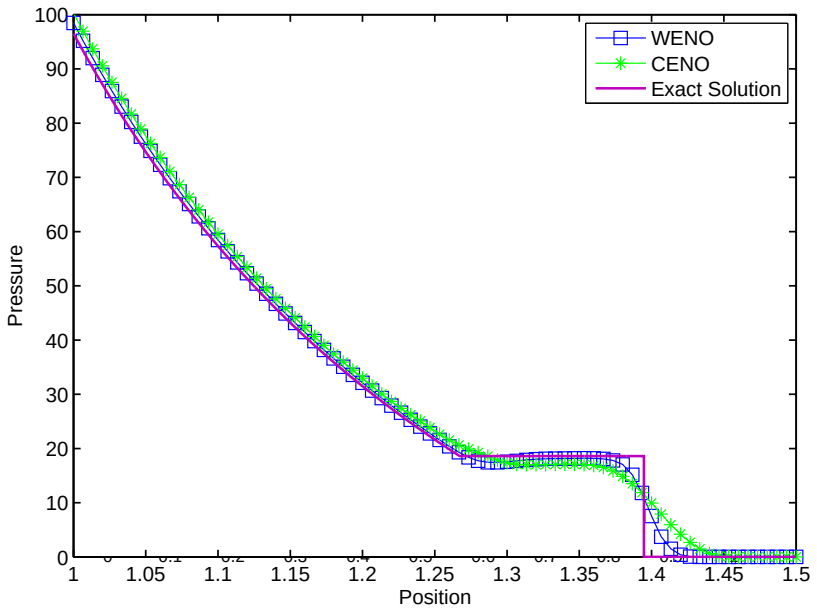

Figure 3.6 Detail from Fig. 3.5 showing the way WENO and CENO reproduce the pressure shock wave.

Fig. 3.6, is especially hard to resolve because has a very small magnitude compared with the scale over which pressure varies in the computational domain.

While WENO does resolve shocks better than CENO for all cases tested, WENO is significantly more computationally expensive than CENO. CENO does not use a spectral decomposition, which make it much faster. The difference in run-times is noticeable even for relatively small grid sizes. Run-times for WENO and CENO are shown in table 3.1 for the initial data shown above with an varying number of points and a constant CFL parameter.

# of Points	WENO	CENO
50	0.298	0.074
100	0.680	0.141
200	2.417	0.548
400	9.232	2.010
800	36.839	7.478
1600	97.418	19.371
3200	391.946	76.022

Table 3.1 Run-times in seconds of WENO and CENO schemes for step function initial data with a constant CFL parameter of 0.4.

3.3 Conclusions

In this thesis, we have investigated the CWENO algorithm without a staggered grid and the WENO algorithm for use in modeling astrophysical systems. We can conclude that CWENO without a staggered grid is weakly unstable for the GRMHD fluid equations and shows increasing error in time when applied to Burger's equation. This

shows that CWENO is unsuitable for solving the GRMHD fluid equations without the use of a staggered grid.

In applying WENO to the GRMHD equations, we immediately face the problem that a numerical implementation for the characteristic decomposition is not known. For the general relativistic perfect fluid equations, we can conclude that WENO resolves discontinuities better than CENO, but is also much more computationally expensive. Therefore WENO may be an effective method for use in modeling a neutron star/balck hole collision if the characteristic decomposition of the GRMHD equations can be formatted for numerical computation.

Index

Bibliography

[1] R. D. Blandford, "The Phenomena of High Energy Astrophysics," Arxiv e-prints astro-ph/0302226 (2003).

[2] R. D. Blanford and R. L. Znajek, "Electromagnetic extraction of energy from Kerr black holes," Mon. Not. R. Astron. Soc. **179,** 433 (1977).

[3] B. Zhang, "Gamma-Ray Bursts in the Swift Era," Chin. J. Astron. Astrophys. **7,** 1 (2007).

[4] Y. Mizuno, P. Hardee, and K. Nishikawa, "3D Relativistic MHD Simulations of Magnetized Spine-Sheath Relativistic Jets," ArXiv e-prints astro-ph/0611190 (2006).

[5] L. Del Zanna, E. Amato, and N. Bucciantini, "Axially symmetric relativistic MHD simulations of Pulsar Wind Nebulae in Supernova Remnants - On the origin of torus and jet-like features," Astron. Astrophys. **421,** 1063 (2004).

[6] Y. Mizuno, K.-I. Nishikawa, S. Koide, P. Hardee, and G. J. Fishman, "RAISHIN: A High-Resolution Three-Dimensional General Relativistic Magnetohydrodynamics Code," Arxiv e-prints astro-ph/0609004 (2006).

[7] M. D. Duez, Y. T. Liu, S. L. Shapiro, M. Shibata, and B. C. Stephens, "Evolution of magnetized, differentially rotating neutron stars: Simulations in full general relativity," Physical Review D **73,** 104015 (2006).

[8] M. Shibata, Y. T. Liu, S. L. Shapiro, and B. C. Stephens, "Magnetorotational collapse of massive stellar cores to neutron stars: Simulations in full general relativity," Physical Review D **74,** 104026 (2006).

[9] B. Giacomazzo and L. Rezzolla, "WhiskyMHD: a new numerical code for general relativistic magnetohydrodynamics," ArXiv e-prints gr-qc/0701109 (2007).

[10] R. Arnowitt, S. Deser, and C. W. Misner, "The Dynamics of General Relativity," Louis Witten, Ed. **7,** 227 (1962).

[11] D. Neilsen, E. W. Hirschmann, and R. S. Millward, "Relativistic MHD and black hole excision: Formulation and initial tests," Class. Quant. Grav. **23,** S505 (2006).

[12] M. Anderson, E. Hirschmann, S. L. Liebling, and D. Neilsen, "Relativistic MHD with Adaptive Mesh Refinement," Class. Quant. Grav. **23,** 6503 (2006).

[13] C. Shu, "Essentially Non-Oscillatory and Weighted Essentially Non-Oscillatory Schemes for Hyperbolic Conservation Laws," Technical report (1997) .

[14] S. Osher and C.-W. Shu, "Essentially non-oscillatory shock capturing methods applied to turbulence amplification in shock wave calculations," NASA STI/Recon Technical Report N **89,** 13732 (1988).

[15] J. Qiu and C.-W. Shu, "On the construction, comparison, and local characteristic decomposition for high-Order central WENO schemes," J. Comput. Phys. **183,** 187–209 (2002).

[16] J. A. Font, M. Miller, W.-M. Suen, and M. Tobias, "Three-dimensional numerical general relativistic hydrodynamics: Formulations, methods, and code tests," Phys. Rev. D **61,** 044011 (2000).

[17] G.-S. Jiang and C.-W. Shu, "Efficent Implementation of Weighted ENO Schemes," J. Comput. Phys. **126,** 202–228 (1996).

[18] S. Vukovic, N. Crnjaric-Zic, and L. Sopta, "WENO schemes for balance laws with spatially varying flux," J. Comput. Phys. **199,** 87–109 (2004).

[19] D. S. Balsara and C.-W. Shu, "Monotonicity Preserving Weighted Essentially Non-oscillatory Schemes with Increasingly High Order of Accuracy," J. Comput. Phys. **160,** 405–452 (2000).